

## 7 Operational discrimination of raining from non-raining clouds in mid-latitudes using multispectral satellite data

Thomas Nauss<sup>1</sup>, Boris Thies<sup>1</sup>, Andreas Turek<sup>1</sup>, Jörg Bendix<sup>1</sup>,  
Alexander Kokhanovsky<sup>2</sup>

<sup>1</sup>Laboratory of Climatology and Remote Sensing, University of Marburg  
Germany

<sup>2</sup>Institute of Remote Sensing, University of Bremen, Germany

### Table of contents

7.1 Introduction .....	169
7.2 Conceptual model for the discrimination of raining from non-raining mid-latitude cloud systems .....	170
7.3 Retrieval of the optical cloud properties using multispectral satellite data .....	171
7.4 Application of the conceptual model to Meteosat Second Generation <i>SEVIRI</i> data .....	173
7.5 Evaluation of the new rain area delineation scheme .....	181
7.6 Conclusions .....	186
7.7 References .....	188

### 7.1 Introduction

The detection of rainfall by geostationary (GEO) weather satellites has a long tradition as they provide area-wide information about the distribution of this key parameter of the water cycle in a very high temporal and high spatial resolution (e.g., Adler and Negri 1988). Most retrieval techniques developed so far for GEO systems are based on the relationship between cloud top temperature in the infrared channel and rainfall probability. Such retrievals which are often referred to as IR retrievals are appropriate for the tropics where precipitation is generally

linked with deep convective clouds that can be easily identified in the infrared and/or water vapour channels (e.g., Levizzani et al. 2001; Levizzani 2003) but show considerable drawbacks in the mid-latitudes (e.g., Ebert et al. 2007, Früh et al. 2007) where great parts of the precipitation originates from clouds preferably formed by spatially extended frontal lifting processes in extra-tropical cyclones (hereafter denoted as advective/stratiform precipitation).

To overcome this drawback, some authors have suggested to use the effective cloud droplet radius ( $a_{ef}$ ) defined as the ratio of the third to the second power of the cloud droplet spectrum (Hansen and Travis 1974) which can be retrieved from multi-spectral satellite data. They propose to use values of  $a_{ef}$  of around  $14\text{ }\mu\text{m}$  as a fixed threshold value (THV) for precipitating clouds (e.g., Rosenfeld and Gutman 1994; Lensky and Rosenfeld 1997; Ba and Gruber 2001) but these studies have mainly focused on convective systems and a fixed THV seems to be not applicable for a reliable differentiation between frontal induced raining and non-raining stratiform clouds over large parts of Europe. In this context, Nauss and Kokhanovsky (2006, 2007) recently proposed a new scheme for the discrimination of raining and non-raining cloud areas applicable to mid-latitudes using daytime multispectral satellite data. Similarly, Thies et al. (2007b) introduced a new technique for rain area delineation in the mid-latitudes using night-time multispectral satellite data. In the following sub-sections, the conceptual model of this new approach as well as its application to geostationary *MSG* (Meteorosat Second Generation) *SEVIRI* (Spinning Enhanced Visible and InfraRed Imager) data will be presented. Since the final technique is different for day- and night-time scenes, the two algorithms will be presented separately.

## 7.2 Conceptual model for the discrimination of raining from non-raining mid-latitude cloud systems

Due to the very homogenous spatial distribution of cloud-top temperature  $T$  for (warm) clouds with values of  $T$  differing not significantly between raining and non-raining regions, the advective/stratiform precipitating cloud area is generally underestimated or even not detected by some of the advanced infrared temperature threshold techniques like the Convective-Stratiform-Technique *CST* (Adler and Negri 1988) or the Enhanced Convective-Stratiform-Technique *ECST* (Reudenbach 2003). Therefore, the authors propose to

use the cloud liquid water path to identify raining clouds in optical satellite data. This idea is based on the conceptual model that rainfall is favoured by both, cloud droplets with sufficiently large diameters where terminal velocity can over-compensate updraft wind fields, and a vertical cloud extent large enough to allow droplets to grow and preventing them from evaporating below the cloud base (which in turn has an influence on the required droplet size; see Lensky and Rosenfeld 2003a). Consequently, precipitating clouds in the new conceptual model must be characterised by a specific combination of droplet size and the cloud thickness, both large enough to form rain droplets. Since neither the droplet spectrum nor the geometrical thickness of a cloud can be computed from optical data without additional theoretical assumptions, the effective droplet radius ( $a_{ef}$ ) and the cloud optical thickness ( $\tau$ ) is used as a proxy for the particle size and the cloud thickness. Multiplying both parameters according to:

$$lwp = \frac{2}{3} \cdot \tau \cdot a_{ef} \quad (1)$$

one gets the liquid water path (lwp) which again is related to the rainfall probability of a cloud so that raining clouds can finally be characterised by a sufficiently large lwp.

The new proposed scheme shows an improvement in rain area delineation compared to existing techniques using only a threshold for cloud top infrared temperature especially for advective/stratiform precipitation clouds.

### 7.3 Retrieval of the optical cloud properties using multispectral satellite data

Values of lwp (i.e., values of  $a_{ef}$  and  $\tau$ ) can be retrieved on a pixel basis during daytime using a combination of two solar channels (e.g., Nakajima and Nakajima 1995; Kawamoto et al. 2001; Kokhanovsky et al. 2003; Kokhanovsky et al. 2005; Platnick et al. 2003; Nauss et al. 2005). This is due to the fact that the reflection of solar light by a cloud in a non-absorbing wavelength (i.e., a visible channel between 0.4 and 0.8  $\mu\text{m}$ ) is strongly correlated to the optical thickness while the reflection of solar light in a slightly absorbing wavelength (i.e., a near-infrared channel between 1.6 and 3.9  $\mu\text{m}$ ) is mainly a function of the cloud effective droplet radius.

To proof the conceptual model presented above within an initial test study, Nauss and Kokhanovsky (2006, 2007) utilize the Semi-

AnalYtical CloUd Retrieval Algorithm (*SACURA*, Kokhanovsky et al. 2003; Kokhanovsky et al. 2005; Nauss et al. 2005) to compute  $a_{\text{ef}}$ ,  $\tau$ , and finally  $l_{\text{wp}}$  using data from NASA's Terra-*MODIS* sensor (Moderate Resolution Imaging Spectroradiometer, <http://modis.gsfc.nasa.gov/>, last access 2007/07/30). *SACURA* is based on asymptotic solutions and exponential approximations of the radiative transfer theory valid for weakly absorbing media (Kokhanovsky and Rozanov 2003, 2004), which are applicable for cloud retrievals up to a wavelength of around  $2.2\mu\text{m}$ . For a single scattering albedo ( $\varpi_0$ ) equal to one, the equations coincide with more general asymptotic formulae valid for all values of  $\varpi_0$  (Germogenova 1963; van de Hulst 1980; King 1987) and differ only insignificantly from general equations as  $\varpi_0 \rightarrow 1$ . However, the exponential approximation provides much simpler final expressions, which can be used as a basis for a high-speed cloud retrieval algorithm necessary for near-realtime applications (Kokhanovsky et al., 2003). *SACURA* has been validated over sea and land surfaces against the commonly used but computer-time expensive look-up table approaches of the Japanese Space Agency JAXA (Nakajima and Nakajima 1995; Kawamoto et al. 2001) and the NASA *MODIS* cloud property product MOD06 (Platnick et al. 2003) showing good agreement for optically thick (e.g., raining) cloud systems (Nauss et al. 2005). However, as *SACURA* is only valid for water clouds it does not consider the ice phase which leads to inaccuracies concerning precipitating clouds in the mid-latitudes as efficient precipitation processes are mainly connected to the ice phase and the so called Bergeron-Findeisen process (e.g., Houze 1993). Recently, Kokhanovsky and Nauss (2005) and Kokhanovsky and Nauss (2006) showed that a fast and accurate calculation of the effective cloud particle radius ( $a_{\text{ef}}$ ) and the cloud optical thickness ( $\tau$ ) is possible for water and ice clouds by using again a non-absorbing visible and an absorbing near infrared channel (e.g.,  $0.8\mu\text{m}$  and  $1.6\mu\text{m}$ ).

Since the cloud microphysical and optical properties are strongly related to the reflection of solar light but not to the emission of the cloud, there is no retrieval at hand that can explicitly compute  $a_{\text{ef}}$  and  $\tau$  during night-time. Anyhow, several case studies have shown that implicit information about  $a_{\text{ef}}$  and  $\tau$  is available in the emissive channels during night-time. Stone et al. (1990), Ou et al. (1993), González et al. (2002), Ou et al. (2002), and Hutchison et al. (2006), used a  $3.7\mu\text{m}$  channel and a  $11\mu\text{m}$  channel combination to infer microphysical and optical cloud properties. The studies of Inoue (1985), Wu (1984), and Baum et al. (1994), have shown that both the brightness temperature differences ( $\Delta T$ ) between a  $3.7\mu\text{m}$  channel and a  $11\mu\text{m}$  channel ( $\Delta T_{3.7-11}$ ).

$_{11}$ ) and between a 11  $\mu\text{m}$  channel and a 12  $\mu\text{m}$  channel ( $\Delta T_{11-12}$ ) are sensitive to the cloud's microphysical and optical properties. Baum et al. (1994) stated that both brightness temperature differences used in combination provide more information regarding cloud properties than either  $\Delta T$  alone. Ackerman et al. (1998a) and Huang et al. (2004) demonstrated the sensitivity of the  $\Delta T$  between a 8.5  $\mu\text{m}$  and 11  $\mu\text{m}$  channel ( $\Delta T_{8.5-10.8}$ ) and  $\Delta T_{11-12}$  to values of  $a_{\text{ef}}$ . Lensky and Rosenfeld (2003a) utilized  $\Delta T_{3.7-11}$  to check a passing criteria indicating the actual cloud geometrical depth and particle size combination is large enough for the pixel to be considered as precipitating.

#### 7.4 Application of the conceptual model to Meteosat Second Generation *SEVIRI* data

With the availability of the *SEVIRI* sensor aboard the new European GEO system Meteosat Second Generation (Aminou 2002; Schmetz et al. 2002; Levizzanni et al. 2001), a system is in orbit which provides a sufficient spectral resolution to infer information about the liquid water path and the ice water path (hereafter both referred to as cloud water path (*cwp*)) as well as about the cloud phase. Furthermore it offers a high temporal (15 minutes) and spatial (3 by 3 km at sub-satellite point) resolution necessary for a continuous area-wide monitoring of the rainfall distribution which is essential for nowcasting purposes. Therefore, the authors chose that system for implementing a new operational technique for the rain area delineation in mid-latitudes on a 15 minute basis for daytime and night-time data.

##### 7.4.1 The daytime approach

As stated in the previous chapter, *SACURA* is only applicable to water clouds. Concerning the rain area delineation in the mid-latitudes this represents a shortcoming as effective precipitation processes in these regions are mainly connected to the ice phase and the so called Bergeron Findeisen process. As a consequence, Kokhanovsky and Nauss (2006) have already presented the fast and accurate forward radiative transfer scheme *CLOUD* which enables the computation of the cloud properties for water and ice clouds using one non-absorbing and one absorbing band available on *MSG SEVIRI*. However, a fast inverse radiative transfer scheme is required for the operational retrieval of cloud properties which is currently under final evaluation. Because this

scheme (called *SLALOM*) is not yet finally approved, the authors decided to use the original reflections of the  $0.56 - 0.71 \mu\text{m}$  ( $\text{VIS}_{0.6}$ ) and  $1.5 - 1.78 \mu\text{m}$  ( $\text{NIR}_{1.6}$ ) *SEVIRI* channels for this study, instead of computed values of  $a_{\text{ef}}$  and  $\tau$ .

Information about the cloud phase are incorporated by means of  $\Delta T_{8.7-10.8}$  and  $\Delta T_{10.8-12.1}$  (refer to Strabala et al. 1994; Ackerman et al. 1998b). The differentiation is based on the observation that the increase of water particle absorption is greater between 11 and 12  $\mu\text{m}$  than between 8 and 11  $\mu\text{m}$ . The ice particle absorption increases more between 8 and 11  $\mu\text{m}$  than between 11 and 12  $\mu\text{m}$  (Strabala et al. 1994). Therefore,  $\Delta T_{10.8-12.1}$  of water clouds are greater than  $\Delta T_{8.7-10.8}$ . On the other hand,  $\Delta T_{8.7-10.8}$  of ice clouds are greater than coincident  $\Delta T_{10.8-12.1}$ .

To use the information about the *cwp* and the cloud phase for a proper detection of potentially precipitating cloud areas (i.e., a large enough *cwp* and ice particles in the upper part of the cloud) the rainfall confidence is calculated as a function of the value combinations of the four variables  $\text{VIS}_{0.6}$ ,  $\text{NIR}_{1.6}$ ,  $\Delta T_{8.7-10.8}$ , and  $\Delta T_{10.8-12.1}$  (e.g., Bellon et al. 1980; Cheng et al. 1993; Kurino 1997; Nauss and Kokhanovsky 2007). The computation of the pixel based rainfall confidence is realized by a comparison of these combinations with ground based radar data from the German Weather Service (DWD 2005) for daytime precipitation events from January to August 2004 (altogether 850 scenes).

Figure 1 shows the calculated rainfall confidence as a function of  $\text{VIS}_{0.6}$  and  $\text{NIR}_{1.6}$  (a), as well as a function of  $\Delta T_{8.7-10.8}$  and  $\Delta T_{10.8-12.1}$  (b). Equation (2) shows the calculation of the rainfall confidences as a function of two different variables.

$$\text{RainConf}(x_1, x_2) = \frac{N_{\text{Rain}}(x_1, x_2)}{N_{\text{Rain}}(x_1, x_2) + N_{\text{NoRain}}(x_1, x_2)} \quad (2)$$

where  $N_{\text{Rain}}$  and  $N_{\text{NoRain}}$  are the raining and the non-raining frequencies, respectively, and  $x_1$  and  $x_2$  denote the channel or channel difference ( $\text{VIS}_{0.6}$ ,  $\text{NIR}_{1.6}$ ,  $\Delta T_{8.7-10.8}$ ,  $\Delta T_{10.8-12.1}$ ) combined for the calculation of the rainfall confidence.

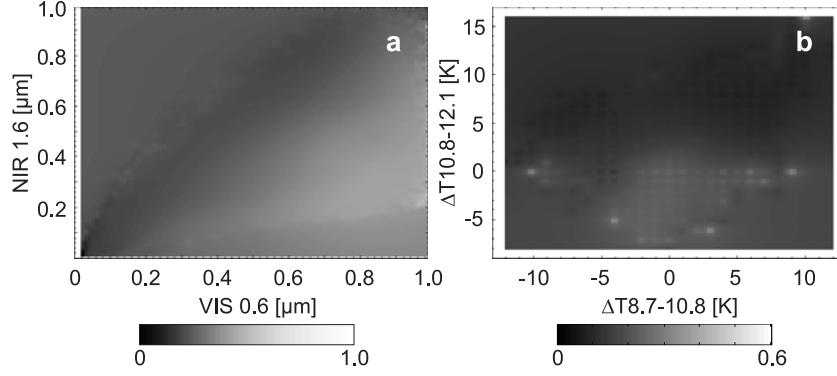


**Fig. 1.** The rainfall confidence as a function of  $VIS_{0.6}$  and  $NIR_{1.6}$  (a), as well as a function of  $\Delta T_{8.7-10.8}$  and  $\Delta T_{10.8-12.1}$  (b) calculated with Eq. (2)

As can be seen in Fig. 1a high values of the rainfall confidence coincide with high values of  $VIS_{0.6}$  and low values of  $NIR_{1.6}$ , indicating a large *cwp*. High values of  $VIS_{0.6}$  indicate a high optical thickness and low values of  $NIR_{1.6}$  indicate large cloud particles as the absorption increases with increasing particle size. Fig. 1b indicates that ice clouds ( $\Delta T_{8.7-10.8} > \Delta T_{10.8-12.1}$ ) possess high rainfall confidences and water clouds ( $\Delta T_{8.7-10.8} < \Delta T_{10.8-12.1}$ ) are characterised by lower rainfall confidences.

To make use of the combined information content in each channel difference for rain delineation, the rainfall confidence is computed as a function of the combined values of the four variables as shown in Eq. (3) using the above mentioned 850 scenes:

$$\text{RainConf}(x_1, x_2, x_3, x_4) = \frac{N_{\text{Rain}}(x_1, x_2, x_3, x_4)}{N_{\text{Rain}}(x_1, x_2, x_3, x_4) + N_{\text{NoRain}}(x_1, x_2, x_3, x_4)} \quad (3)$$

where  $N_{\text{Rain}}$  and  $N_{\text{NoRain}}$  are the raining and the non-raining frequencies, respectively, and  $x_1, x_2, x_3$ , and  $x_4$  denote the channel or channel difference ( $VIS_{0.6}$ ,  $NIR_{1.6}$ ,  $\Delta T_{8.7-10.8}$ ,  $\Delta T_{10.8-12.1}$ ) combined for the calculation of the rainfall confidence.

The threshold of the calculated rainfall confidence appropriate for rain area delineation is determined by optimising the equitable threat score (ETS) which is based on the number of pixels that have been identified by the satellite (S) and radar (R) techniques as raining ( $S_Y, R_Y$ ) or non-raining ( $S_N, R_N$ ). It indicates how well the classified rain pixels correspond to the rain pixels observed by the radar, also accounting for pixels correctly classified by chance ( $S_Y R_Y \text{Random}$ ). Its

value can range from  $-1/3$  to 1 with the optimum value 1. The ETS is calculated according to

$$ETS = \frac{S_Y R_Y - S_Y R_{YRandom}}{S_Y R_Y + S_N R_Y + S_Y R_N - S_Y R_{YRandom}} \quad (4)$$

with

$$S_Y R_{YRandom} = \frac{(S_Y R_Y + S_N R_Y) \cdot (S_Y R_Y + S_Y R_N)}{T_{SR}} \quad (5)$$

where  $T_{SR}$  denotes the total number of pixels.

Different rainfall confidence threshold values between 0.1 and 0.7 were used to delineate the satellite-based rain area. The ETS for the delineated rain areas based on the different rainfall confidence levels were calculated again in comparison with ground based radar data. The delineated rain area using a rainfall confidence threshold of 0.34 yields to the optimised ETS of 0.24. Therefore, the rainfall confidence of 0.34 is chosen as the minimum threshold for precipitating clouds during daytime.

#### 7.4.2 The night-time approach

As already mentioned above, no operational technique is currently at hand to compute the cloud water path based on the cloud emissions during night-time. However, based on the findings mentioned in Sect. 7.3, the brightness temperature differences between the following *SEVIRI* channel differences are considered to gain implicit information on the cloud water path as well as on the cloud phase to detect potentially precipitating cloud areas:

- $\Delta T_{3.9-10.8}$ :  $\Delta T$  between the 3.9  $\mu m$  channel (3.48 - 4.36  $\mu m$ ) and the 10.8  $\mu m$  channel (9.8 - 11.8  $\mu m$ )
- $\Delta T_{3.9-7.3}$ :  $\Delta T$  between the 3.9  $\mu m$  channel and the 7.3  $\mu m$  channel (6.85 - 7.85  $\mu m$ )
- $\Delta T_{8.7-10.8}$ :  $\Delta T$  between the 8.7  $\mu m$  channel (8.3 - 9.1  $\mu m$ ) and the 10.8  $\mu m$  channel
- $\Delta T_{10.8-12.1}$ :  $\Delta T$  between the 10.8  $\mu m$  channel and the 12.1  $\mu m$  channel (11 - 13  $\mu m$ )

Regarding  $\Delta T_{3.9-10.8}$ , a large *cwp* is the product of a large effective



particle radius and a high optical thickness. Large particles have a higher emission in the 3.9  $\mu\text{m}$  channel compared to smaller particles. This is due to the increased scattering of smaller particles which reduces the cloud emissivity. As a result, the brightness temperature in the 3.9  $\mu\text{m}$  channel is higher for larger particles. This dependence on particle size is much less distinct in the 10.8  $\mu\text{m}$  channel. Therefore,  $\Delta T_{3.9-10.8}$  is higher for larger particles. For optically thin clouds the emission in the 3.9  $\mu\text{m}$  channel is less than in the 10.8  $\mu\text{m}$  channel. As a result, the 3.9  $\mu\text{m}$  transmittance is larger than the 10.8  $\mu\text{m}$  transmittance, which implies a larger transmissivity of below-cloud radiance of the former wavelength (see Lensky and Rosenfeld 2003b). Thus, for optically thin clouds consisting of small or large particles (small or medium *cwp*), the brightness temperature of the 3.9  $\mu\text{m}$  channel is larger than that of the 10.8  $\mu\text{m}$  channel and  $\Delta T_{3.9-10.8}$  reaches the highest values. Large particles together with a high optical thickness (large *cwp*) result in medium to high difference values but these differences are always lower than for optically thin clouds. Thick clouds with small particles (medium *cwp*) lead to small  $\Delta T_{3.9-10.8}$ .

In General,  $\Delta T_{3.9-7.3}$  should show similar characteristics as  $\Delta T_{3.9-10.8}$ . Because of the diminishing effect of the water vapour absorption and emission in mid- to low tropospheric levels on the brightness temperature (BT) in the 7.3  $\mu\text{m}$  channel ( $BT_{7.3}$ ) (Schmetz et al. 2002),  $\Delta T_{3.9-7.3}$  should be generally higher than  $\Delta T_{3.9-10.8}$ . Therefore,  $\Delta T_{3.9-7.3}$  is expected to provide additional information about the cloud water path. For thin clouds with small or large particles, respectively (small or medium *cwp*),  $BT_{3.9}$  is larger than  $BT_{7.3}$  and  $\Delta T_{3.9-7.3}$  reaches the highest values. Large particles together with a high optical thickness (high *cwp*) result in medium to high difference values which are lower than for optically thin clouds. Thick clouds with small particles (medium *cwp*) lead to small  $\Delta T_{3.9-7.3}$ .

Concerning  $\Delta T_{8.7-10.8}$  cloud radiative properties in both channels are dependent upon the cloud particle size. Scattering processes and the dependence on particle size are stronger in the 8.7  $\mu\text{m}$  channel relative to the 10.8  $\mu\text{m}$  channel (Strabala et al. 1994). Therefore, for larger particles  $\Delta T_{8.7-10.8}$  increases. The water vapour absorption in the 8.7  $\mu\text{m}$  channel is higher relative to the 10.8  $\mu\text{m}$  channel (Soden and Bretherton 1996; Schmetz et al. 2002). This is why  $\Delta T_{8.7-10.8}$  is lower for low optical thicknesses. For higher optical thicknesses,  $\Delta T_{8.7-10.8}$  increases. As a result,  $\Delta T_{8.7-10.8}$  reaches high values for large effective particle radii and large optical thicknesses (large *cwp*). A low optical thickness in combination with small effective particle radii (small *cwp*) lead to minimum  $\Delta T_{8.7-10.8}$ . A low optical thickness with large

particles (medium *cwp*) and a large optical thickness with small particles (medium *cwp*) result in medium values of  $\Delta T_{8.7-10.8}$ .

$\Delta T_{10.8-12.1}$  is positive at low optical thicknesses due to the increased water vapour absorption in the 12.1  $\mu\text{m}$  channel relative to the 10.8  $\mu\text{m}$  channel. For higher optical thicknesses  $\Delta T_{10.8-12.1}$  decreases as the transmittance and the influence of water vapour emission from beneath diminish (Inoue 1987; Baum et al. 1994). Particle absorption at 10.8  $\mu\text{m}$  and 12.1  $\mu\text{m}$  decreases with increasing effective radius. An increase in particle size acts to decrease  $\Delta T_{10.8-12.1}$  (Baum et al. 1994). As a result,  $\Delta T_{10.8-12.1}$  reaches lowest values for large particles and large optical thicknesses (large *cwp*). Highest values for  $\Delta T_{10.8-12.1}$  are characteristic for low optical thicknesses together with small effective particle radii (small *cwp*). Medium values for  $\Delta T_{10.8-12.1}$  are reached for high optical thicknesses together with small effective particle radii (medium *cwp*) as well as for low optical thicknesses in combination with a large effective particle radius (medium *cwp*).

The effect of the *cwp* on the respective channel difference is summarized in table 1. High  $\Delta T_{3.9-10.8}$  together with high  $\Delta T_{3.9-7.3}$  correspond to small *cwp*. Highest values for both  $\Delta T$  correspond to medium *cwp*. Medium  $\Delta T_{3.9-10.8}$  and  $\Delta T_{3.9-7.3}$  are indicative for large *cwp*. Low  $\Delta T_{3.9-10.8}$  and low  $\Delta T_{3.9-7.3}$  are the result of a medium *cwp*. High (highest)  $\Delta T_{3.9-10.8}$  together with low  $\Delta T_{8.7-10.8}$  correspond to small (medium) *cwp*. Medium  $\Delta T_{3.9-10.8}$  and high  $\Delta T_{8.7-10.8}$  refer to large *cwp*. Low  $\Delta T_{3.9-10.8}$  and medium  $\Delta T_{8.7-10.8}$  are indicative for medium *cwp*. The same statements hold true for  $\Delta T_{3.9-7.3}$  and  $\Delta T_{8.7-10.8}$  in combination. High (highest)  $\Delta T_{3.9-10.8}$  and high  $\Delta T_{10.8-12.1}$  are the result of small (medium) *cwp*. Medium  $\Delta T_{3.9-10.8}$  together with low to medium  $\Delta T_{10.8-12.1}$  refer to large *cwp*. Low  $\Delta T_{3.9-10.8}$  and medium  $\Delta T_{10.8-12.1}$  correspond to medium *cwp*. The same features are characteristic for  $\Delta T_{3.9-7.3}$  and  $\Delta T_{10.8-12.1}$  in combination. Low  $\Delta T_{8.7-10.8}$  together with high  $\Delta T_{10.8-12.1}$  are indicative for small *cwp*. High  $\Delta T_{8.7-10.8}$  and low  $\Delta T_{10.8-12.1}$  correspond to large *cwp*. Medium  $\Delta T_{8.7-10.8}$  and medium  $\Delta T_{10.8-12.1}$  refer to medium *cwp*.

The rainfall confidence as a function of two different channel differences calculated with Eq. (2) is depicted in Fig. 2. The computation of the pixel based rainfall confidence is analogous to the daytime scheme and is done by a comparison of the *SEVIRI* channel differences with ground based radar data for night-time precipitation events from January to August 2004 (altogether 709 scenes).

**Table 1.** The effect of the cloud water path ( $cwp$ ) on the respective channel difference

	$\Delta T_{3.9-10.8}$	$\Delta T_{3.9-7.3}$	$\Delta T_{8.7-10.8}$	$\Delta T_{10.8-12.1}$
small $cwp$ (small $\tau$ with small $a_{ef}$ )	high	high	low	high
medium $cwp$ (small $\tau$ with large $a_{ef}$ )	highest	highest	medium	medium
medium $cwp$ (large $\tau$ with small $a_{ef}$ )	low	low	medium	medium
large $cwp$ (large $\tau$ with large $a_{ef}$ )	medium	medium	high	low

For the combination of  $\Delta T_{3.9-10.8}$  with  $\Delta T_{3.9-7.3}$  (Fig. 2a) high rainfall confidences can be found for small  $\Delta T_{3.9-10.8}$  and small  $\Delta T_{3.9-7.3}$  as well as for medium  $\Delta T_{3.9-10.8}$  and medium  $\Delta T_{3.9-7.3}$ . These intervals coincide with those for medium to large  $cwp$  (refer to table 1). Low rainfall confidences are characterised by high  $\Delta T_{3.9-10.8}$  and high  $\Delta T_{3.9-7.3}$  which correspond to low  $cwp$  (refer to table 1).

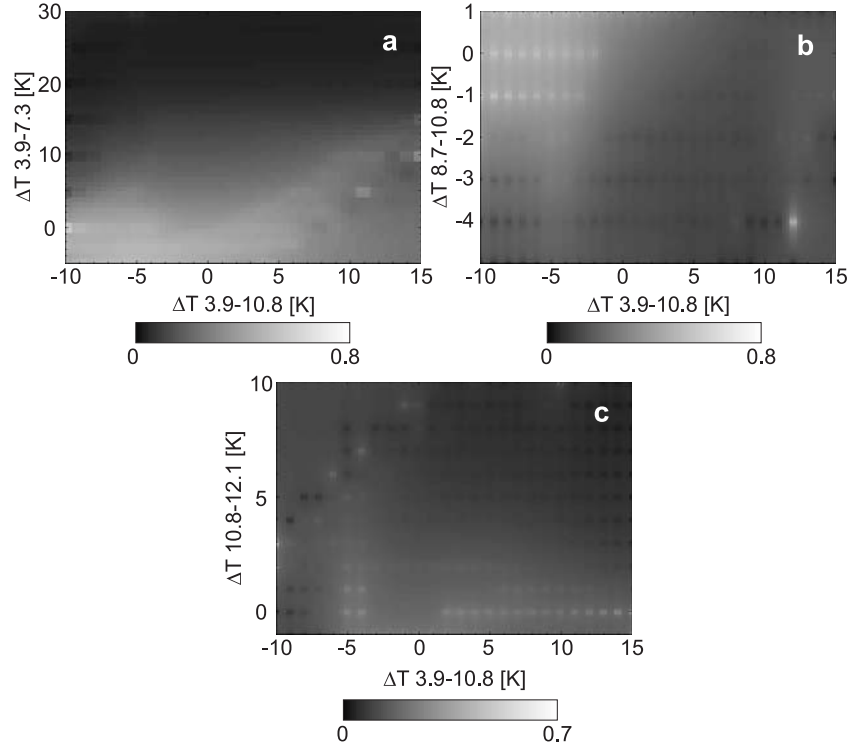


**Fig. 2.** The rainfall confidence as a function of  $\Delta T_{3.9-10.8}$  versus  $\Delta T_{3.9-7.3}$  (a),  $\Delta T_{3.9-10.8}$  versus  $\Delta T_{8.7-10.8}$  (b),  $\Delta T_{3.9-10.8}$  versus  $\Delta T_{10.8-12.1}$  (c) calculated with Eq. (2)

Regarding the combination of  $\Delta T_{3.9-10.8}$  with  $\Delta T_{8.7-10.8}$  (Fig. 2b), high rainfall confidences are indicated for small  $\Delta T_{3.9-10.8}$  and medium  $\Delta T_{8.7-10.8}$  as well as for medium  $\Delta T_{3.9-10.8}$  and large  $\Delta T_{8.7-10.8}$ . Both value intervals correspond to medium and large *cwp* (refer to Fig. 1b). Low rainfall confidences can be found for high  $\Delta T_{3.9-10.8}$  and small  $\Delta T_{8.7-10.8}$  which coincide with low *cwp* (refer to table 1). Concerning the combination of  $\Delta T_{3.9-10.8}$  and  $\Delta T_{10.8-12.1}$  (Fig. 2c) high rainfall confidences are indicated for small  $\Delta T_{3.9-10.8}$  and medium  $\Delta T_{10.8-12.1}$  as well as for medium  $\Delta T_{3.9-10.8}$  and small  $\Delta T_{10.8-12.1}$  which coincide with medium to large *cwp* (refer to table 1). Low rainfall confidences can be found for high  $\Delta T_{3.9-10.8}$  and high  $\Delta T_{10.8-12.1}$  which correspond to low *cwp* (refer to Table 1).

To summarize, it can be stated that intervals of the channel differences representative for high rainfall confidences correspond with the intervals indicative for medium to large *cwp*. This corroborates our conceptual model that clouds with a large enough *cwp* together with ice

particles in the upper parts possess a high probability to produce precipitation.

To make use of the combined information content in each channel difference for rain delineation, the rainfall confidence is computed as a function of the combined values of the four channel differences as shown in Eq. (3) using the above mentioned 709 scenes. The threshold of the rainfall confidence appropriate for rain area delineation is determined analogously to the daytime scheme by optimising the ETS. The delineated rain area using a rainfall confidence threshold of 0.35 yields to the optimised ETS of 0.25. Therefore, the rainfall confidence of 0.35 is chosen as the minimum threshold for precipitating clouds during night-time.

## **7.5 Evaluation of the new rain area delineation scheme**

In order to get an idea of the reliability of the new Rain Area Delineation Scheme for daytime and night-time (*RADS-DN*), 720 day- and 676 night-time precipitation scenes between January and August 2004 have been evaluated. The rainfall events within these scenes are independent of the above mentioned precipitation events used for the algorithm development.

To evaluate the potential improvement by the new *RADS-DN*, the validation scenes were also classified by the Enhanced Convective Stratiform Technique (*ECST*, Reudenbach 2003; Reudenbach et al. 2001) which is similar to the Convective Stratiform Technique (*CST*) of Adler and Negri (1988) but additionally includes the water vapour channel temperature for a more reliable deep convective/cirrus clouds discrimination (see also Tjemkes et al. 1997). The *ECST* which was first transferred from *Meteosat-7 MVIRI* (Meteosat Visible and InfraRed Imager radiometer) to *MSG SEVIRI* (Thies et al. 2007a) is used for the identification of convective rain areas since these regions approximately represent the performance of many present IR rainfall retrievals.

Standard verification scores following the suggestions of the CGMS International Precipitation Working Group (IPWG, Turk and Bauer 2006) were calculated on a pixel basis for each scene in comparison with corresponding ground based radar data from the German Weather Service ( $S_Y$  and  $R_Y$  represent the sum of pixels identified as raining in the satellite and radar product respectively;  $S_N$  and  $R_N$  represent the sum of pixels identified as non-raining). Thereby,

the bias describes the ratio between  $S_Y$  and  $R_Y$ , the probability of detection (POD) the ratio between  $S_Y R_Y$  and the sum of  $S_Y R_Y$  and  $S_N R_Y$ , the probability of false detection (POFD) the ratio between  $S_Y R_N$  and the sum of  $S_Y R_N$  and  $S_N R_N$ , and the false alarm ratio (FAR) the ratio between  $S_Y R_N$  and the sum of  $S_Y R_Y$  and  $S_Y R_N$ . The critical success index (CSI), which encloses all pixels that have been identified as raining by either the radar network or the satellite technique, describes the ratio between  $S_Y R_Y$  and the sum of  $S_Y R_Y$ ,  $S_N R_Y$ , and  $S_Y R_N$ . All scores except the bias range from 0 to 1 and the optimum value for the POD, CSI, and bias is 1, while it is 0 for the POFD and FAR. Since the POD can be increased by just increasing the satellite rainfall area (i.e., by reducing the rainfall confidence threshold), it has to be analysed in connection with corresponding values of the FAR and the POFD since both measure the fraction of the satellite pixels that have been incorrectly identified as raining. The verification scores were calculated on a pixel basis for each single scene without any spatio-temporal aggregation. For a detailed discussion of the verification scores see Stanski et al. (1989) or the web site of the WWRP/WGNE.

### 7.5.1 Evaluation study using daytime scenes

The verification scores calculated for the 720 daytime validation scenes are summarized in Table 2. *RADS-D* slightly overestimates the rain area detected by the radar network which is indicated by the bias of 1.15 (see Table 2). In contrast to this, the rain area is strongly underestimated by the *ECST* (bias of 0.22). 61% of the radar observed raining pixels are also identified by *RADS-D*. This indicates a much better performance compared to the *POD* of 9% for the *ECST*, even if this coincide with a higher *POFD* of 0.18 for *RADS-D* in comparison to 0.04 for the *ECST*. Anyhow, the *FAR* indicates that a lower fraction of the pixels where misclassified as rain by *RADS-D* (0.46) than by the *ECST* (0.51). Altogether, the good performance of the new *RADS-D* is further supported by the *CSI* (0.39) and the *ETS* (0.25). Compared to *ECST* (*CSI*: 0.1; *ETS*: 0.06) this signifies a marked improvement concerning the delineated rain area.

An overview of the performance of *RADS-D* in comparison to the *ECST* is given by the relative operation characteristic (*ROC*) plot in Fig. 3. The visual impression additionally supports the good and improved performance of the new developed scheme. The combination of medium to high values for *POD* together with low to medium values for *POFD* which is valid for the main part of the classified scenes underlines the

overall good skill of the new scheme. In contrast, for scenes classified by the *ECST* the *POD* and *POFD* indicate much lower or even no skills.

**Table 2.** Results of the standard verification scores applied to the rain-area identified by *RADS-D* and *ECST* on a pixel basis. The scores are based on 676 precipitation scenes with 24,914,160 pixels of which 5,872,220 have been identified as raining by *RADS-D*

Test	<i>RADS-D</i>				<i>ECST</i>			
	Mean	StDev	Min	Max	Mean	StDev	Min	Max
Bias	1.15	0.38	0.16	2.17	0.22	0.27	0.0	2.82
<i>POD</i>	0.61	0.21	0.12	0.98	0.12	0.17	0.0	0.97
<i>POFD</i>	0.18	0.09	0.02	0.54	0.04	0.05	0.0	0.78
<i>FAR</i>	0.46	0.12	0.03	0.84	0.51	0.27	0.0	1.0
<i>CSI</i>	0.39	0.14	0.1	0.77	0.1	0.14	0.0	0.64
ETS	0.25	0.11	-0.04	0.53	0.06	0.09	-0.05	0.39

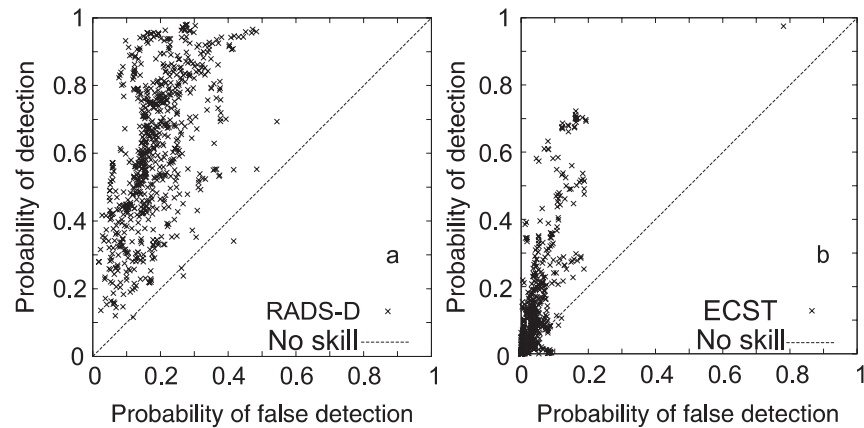


**Fig. 3.** ROC curves for the comparison between *RADS-D* and ground based radar (a), and *ECST* and ground based radar (b). The calculated probability of detection (*POD*) and probability of false detection (*POFD*) are based on the 720 scenes mentioned in the text

To gain a visual impression of the performance of the new developed rain area delineation scheme, the classified rain area for a scene from 12 January 2004 12:45 UTC is depicted in Fig. 4. Figure 4a shows the brightness temperature in the 10.8  $\mu\text{m}$  channel ( $\text{BT}_{10.8}$ ), Fig. 4b the rain area delineated by *RADS-D* as well as by *ECST*, and Fig. 4c the rain area detected by *RADS-D* in comparison to the radar data.

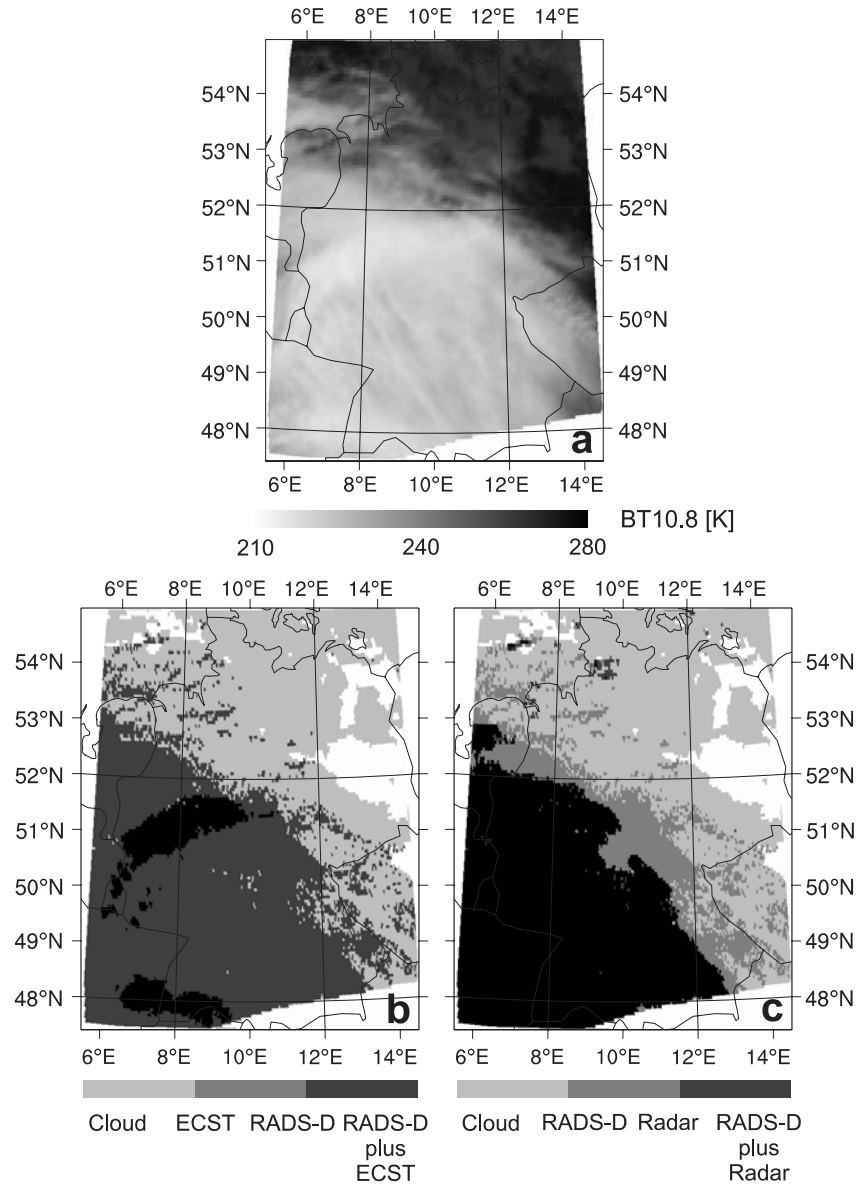


**Fig. 4.** Delineated rain area for the scene from 12 January 2004 12:45 UTC. Figure 4a shows the BT<sub>10.8</sub> image, Fig. 4b the rain area delineated by *RADS-D* as well as by *ECST*, and Fig. 4c the rain area detected by *RADS-D* in comparison to the radar data



### 7.5.2 Evaluation study using night-time scenes

The verification scores calculated for the 676 night-time validation scenes are summarized in Table 3. Compared to the strong underestimation of the rain area by the *ECST*, *RADS-N* moderately overestimates the rain area detected by the radar network which is indicated by the bias of 0.21 for the *ECST* and of 1.4 for *RADS-N* (see Table 3). The *POD* shows that 68% of the radar observed raining pixels are also identified by *RADS-N* which points to a much better performance compared to 9% for the *ECST*, even if this coincide with a higher *POFD* of 0.24 for *RADS-N* in comparison to 0.04 for the *ECST*. However, the false alarm ratio shows that a lower fraction of the pixels where wrongly classified as rain by *RADS-N* (0.52) than by the *ECST* (0.57). The overall good performance of *RADS-N*, indicated by the good range of the verification scores is further supported by the *CSI* (0.37) and the *ETS* (0.22) which outperform the results of the *ECST* (*CSI*: 0.07; *ETS*: 0.03).

**Table 3.** Results of the standard verification scores applied to the rain-area identified by *RADS-N* and *ECST* on a pixel basis. The scores are based on 676 precipitation scenes with 23,392,304 pixels of which 4,746,069 have been identified as raining by *RADS-N*

Test	<i>RADS-N</i>				<i>ECST</i>			
	Mean	StDev	Min	Max	Mean	StDev	Min	Max
Bias	1.42	0.67	0.16	4.97	0.21	0.36	0.0	4.28
<i>POD</i>	0.62	0.18	0.12	0.97	0.09	0.14	0.0	0.95
<i>POFD</i>	0.24	0.13	0.01	0.84	0.04	0.08	0.0	0.94
<i>FAR</i>	0.52	0.14	0.11	0.88	0.57	0.32	0.0	1.0
<i>CSI</i>	0.37	0.13	0.1	0.74	0.07	0.1	0.0	0.53
<i>ETS</i>	0.22	0.12	-0.03	0.57	0.03	0.06	-0.06	0.35

The relative operation characteristic (*ROC*) plot in Fig. 5 gives an overview of the performance of *RADS-N* in comparison to the *ECST*. It underlines again the good performance of the new developed scheme and the improvement in comparison to the *ECST*. For the main part of the classified scenes the *POD* and *POFD* indicate a good skill with medium to high values for *POD* together with low to medium values for *POFD*. In contrast, for scenes classified by the *ECST* the *POD* and *POFD* indicate much lower or even no skills.

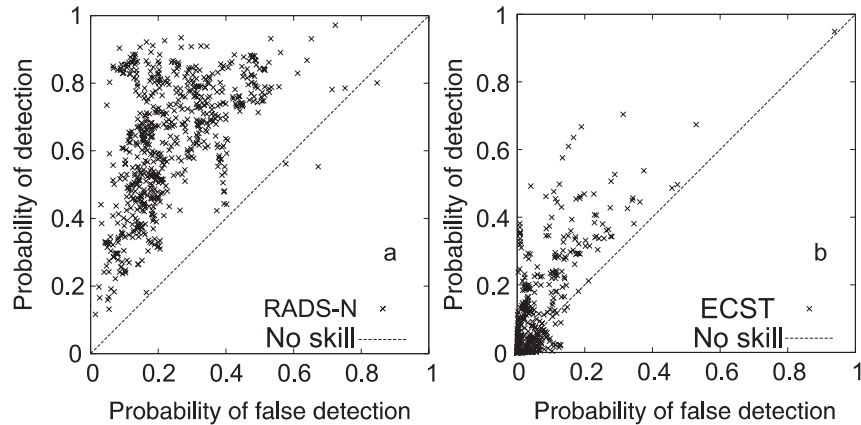


**Fig. 5.** ROC curves for the comparison between *RADS-N* and ground based radar (a), and *ECST* and ground based radar (b). The calculated probability of detection (*POD*) and probability of false detection (*POFD*) are based on the 676 scenes mentioned in the text

To gain a visual impression of the performance of the new developed rain area delineation scheme, the classified rain area for a scene from 31 May 2004 00:45 UTC is depicted in Fig. 6. Figure 6a shows the brightness temperature in the  $10.8\ \mu\text{m}$  channel ( $\text{BT}_{10.8}$ ), Fig. 6b the rain area delineated by *RADS-N* as well as by *ECST*, and Fig. 6c the rain area detected by *RADS-N* in comparison to the radar data.

## 7.6 Conclusions

A new algorithm for rain area delineation during day- and night-time using multispectral optical satellite data of *MSG SEVIRI* was proposed. The method allows not only a proper detection of mainly convective precipitation by means of the commonly used connection between infrared cloud top temperature and rainfall probability but also enables the detection of advective/stratiform precipitation (e. g., in connection with mid-latitude frontal systems). It is based on the new conceptual model that precipitation is favoured by a large cloud liquid or ice water path and the presence of ice particles in the upper part of the cloud.

The daytime technique considers the  $\text{VIS}_{0.6}$  and the  $\text{NIR}_{1.6}$  channel to gain information about the cloud water path. The night-time technique considers information about the cloud water path inherent in

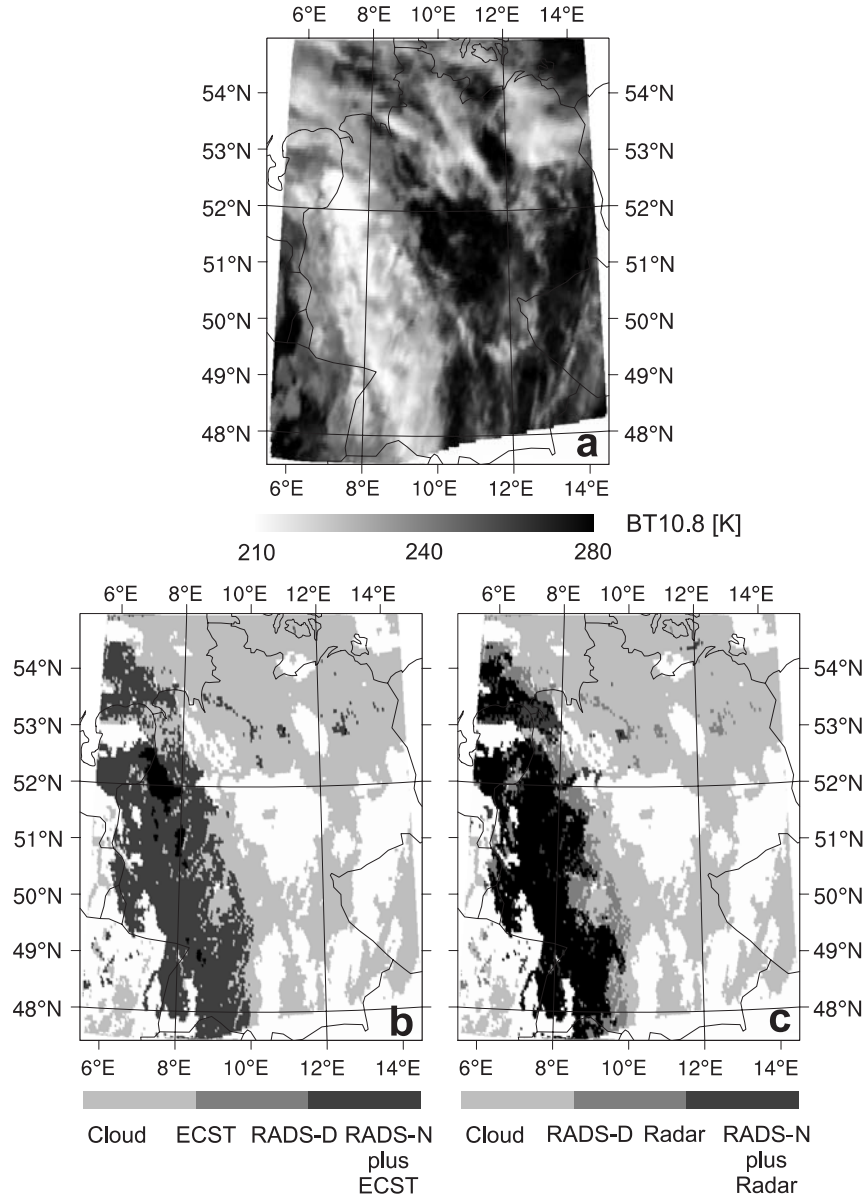


**Fig. 6.** Delineated rain area for the scene from 31 May 2004 00:45 UTC. Figure 6a shows the  $BT_{10.8}$  image, Fig. 6b the rain area delineated by *RADS-N* as well as by *ECST*, and Fig. 6c the rain area detected by *RADS-N* in comparison to the radar data

the channel differences  $\Delta T_{3.9-10.8}$ ,  $\Delta T_{3.9-7.3}$ ,  $\Delta T_{8.7-10.8}$ , and

$\Delta T_{10.8-12.1}$ . Additionally, both techniques utilize the channel differences  $\Delta T_{8.7-10.8}$  and  $\Delta T_{10.8-12.1}$  to gain information about the cloud phase.

The information about the *cwp* and the cloud phase inherent in the four variables is merged and incorporated into the new developed rain area delineation algorithm. Rain area delineation is realized by using the pixel based rainfall confidence as a function of the respective value combination of the four variables. The calculation of the rainfall confidence is based on a comparison of the value combinations of the four variables with ground based radar data. A minimum threshold for the rainfall confidence of 0.34 for the daytime scheme and of 0.35 for the night-time scheme was determined as appropriate for rain area delineation.

The results of the algorithm were compared with corresponding ground based radar. The proposed technique performs better than existing optical retrieval techniques using only IR thresholds for cloud top temperature.

The new developed algorithm shows encouraging performance concerning precipitation delineation during daytime and night-time in the mid-latitudes using *MSG SEVIRI* data and offers the great potential for a 24 h technique for rain area delineation with a high spatial and temporal resolution.

## Acknowledgements

The current study is partly funded by the German Ministry of Research and Education (BMBF) in the framework of GLOWA-Danube project (G-D/2004/TP-10, precipitation/remote sensing) as well as by the German Research Council DFG (BE 1780/18-1) within the SORT project.

The authors are grateful to the German weather service (DWD) for providing the radar datasets within the Eumetsat/DWD Advanced Multisensor Precipitation Experiment (AMPE).

## 7.7 References

- Ackerman SA, Moeller CC, Strabala KI, Gerber HE, Gumley LE, Menzel WP, Tsay SC (1998a) Retrieval of effective microphysical properties of clouds: A wave cloud case study. *Geophys Res Lett* 25:1121-1124
- Ackerman SA, Strabala KI, Menzel WP, Frey RA, Moeller CC, Gumley LE (1998b) Discriminating clear sky from clouds with MODIS. *J Geophys*

- Res-Atmos 103: 32141-32157
- Adler RF, Negri AJ (1988) A satellite technique to estimate tropical convective and stratiform rainfall. *J Appl Meteorol* 27:30-51
- Aminou DMA (2002) MSG's SEVIRI instrument. *ESA Bulletin* 111: 15-17
- Ba MB, Gruber A (2001) GOES Multispectral Rainfall Algorithm (GMSRA). *J Appl Meteorol* 40: 1500-1514
- Baum BA, Arduini RF, Wielicki BA, Minnis P, Tsay SC (1994) Multilevel cloud retrieval using multispectral HIRS and AVHRR data: Night-time oceanic analysis. *J Geophys Res-Atmos* 99: 5499-5514
- Bellon A, Lovejoy S, Austin GL (1980) Combining satellite and radar data for the short-range forecasting of precipitation. *Mon Weather Rev* 108: 1554-1556
- Cheng M, Brown R, Collier CG (1993) Delineation of precipitation areas by correlation of METEOSAT visible and infrared data in the region of the United Kingdom. *J Appl Meteorol* 32: 884-898
- DWD (2005) Weather radar network. Available online at [http://www.dwd.de/en/Technik/Datengewinnung/Radarverbund/Radarbrochure\\_en.pdf](http://www.dwd.de/en/Technik/Datengewinnung/Radarverbund/Radarbrochure_en.pdf). 11 May 2007.
- Ebert EE, Janowiak JE, Kidd C (2007) Comparison of near-real-time precipitation estimates from satellite observations and numerical models. *B Am Meteorol Soc* 88: 47-64
- Früh B, Bendix J, Nauss T, Paulat M, Pfeiffer A, Schipper JW, Thies B, Wernli H (2007) Verification of precipitation from regional climate simulations and remote-sensing observations with respect to ground-based observations in the upper Danube catchment. *Meteorol Z* 16: 275-293
- Germogenova TA (1963) Some formulas to solve the transfer equation in the plane layer problem. In: B. I. Stepanov (Ed.): *Spectroscopy of Scattering Media*. Academy of Sciences of BSSR, Minsk, pp 36-41
- González A, Pérez JC, Herrera F, Rosa F, Wetzel MA, Borys RD, Lowenthal DH (2002) Stratocumulus properties retrieval method from NOAA-AVHRR data based on the discretization of cloud properties. *Int J Remote Sens* 23: 627-645
- Hansen JE, Travis LD (1974) Light scattering in planetary atmospheres. *Space Sci Rev* 16: 527-610
- Houze RA (1993) *Cloud Dynamics*. Vol. 53 of the International Geophysics Series. Academic Press. San Diego
- Huang HL, Yang P, Wei HL, Baum BA, Hu YX, Antonelli P, Ackerman SA (2004) Inference of ice cloud properties from high spectral resolution infrared observations. *IEEE T Geosci Remote* 42:842-853
- Hutchison K, Wong E, Ou SC (2006) Cloud base heights retrieved during night-time conditions with MODIS data. *Int J Remote Sens* 27: 2847-2862
- Inoue T (1985) On the temperature and effective emissivity determination of semi-transparent cirrus clouds by bi-spectral measurements in the 10  $\mu\text{m}$  window region. *J Meteorol Soc Jpn* 63: 88-98
- Inoue T (1987) An instantaneous delineation of convective rainfall areas using split window data of NOAA-7 AVHRR. *J Meteorol Soc Jpn* 65: 469-481

- Kawamoto K, Nakajima T, Nakajima TY (2001) A global determination of cloud microphysics with AVHRR remote sensing. *J Climate* 14: 2054-2068
- King MD (1987) Determination of the scaled optical thickness of clouds from reflected solar radiation measurements. *J Atmos Sci* 44: 1734-1751
- Kokhanovsky AA, Rozanov VV (2004) The physical parameterization of the top-of-atmosphere reflection function for a cloudy atmosphere-underlying surface system: the oxygen A-band case study. *J Quant Spectrosc Ra* 85: 35-55
- Kokhanovsky AA, Rozanov VV (2003) The reflection function of optically thick weakly absorbing turbid layers: a simple approximation. *J Quant Spectrosc Ra* 77: 165-175
- Kokhanovsky AA, Nauss T (2006) Reflection and transmission of solar light by clouds: asymptotic theory. *Atmos Chem Phys* 6: 5537-5545
- Kokhanovsky AA, Nauss T (2005) Satellite-based retrieval of ice cloud properties using a semi-analytical algorithm. *J Geophys Res-Atmos* 110/D19 : D19206, doi:10.1029/2004JD005744
- Kokhanovsky AA, Rozanov VV, Nauss T, Reudenbach C, Daniel JS, Miller HL, Burrows JP (2005) The semianalytical cloud retrieval algorithm for SCIAMACHY. I: The validation. *Atmos Chem Phys* 6: 1905-1911
- Kokhanovsky AA, Rozanov VV, Zege EP, Bovensmann H, Burrows JP (2003) A semi-analytical cloud retrieval algorithm using backscattered radiation in 0.4–2.4 micrometers spectral range. *J Geophys Res-Atmos* 108(D1): 4008, doi:10.1029/2001JD001543.
- Kurino T (1997) A satellite infrared technique for estimating 'deep/shallow' precipitation. *Adv Space Res* 19: 511-514
- Lensky IM, Rosenfeld D (1997) Estimation of precipitation area and rain intensity based on the microphysical properties retrieved from NOAA AVHRR data. *J Appl Meteorol* 36: 234-242
- Lensky IM, Rosenfeld D (2003a) A night-time delineation algorithm for infrared satellite data based on microphysical considerations. *J Appl Meteorol* 42:1218-1226
- Lensky IM, Rosenfeld D (2003b) Satellite-based insights into precipitation formation processes in continental and maritime convective clouds at night-time. *J Appl Meteorol* 42: 1227-1233
- Levizzani V (2003) Satellite rainfall estimations: new perspectives for meteorology and climate from the EURAINSAT project. *Ann Geophys-Italy* 46:363-372
- Levizzani V, Schmetz J, Lutz HJ, Kerkmann J, Alberoni PP, Cervino M (2001) Precipitation estimations from geostationary orbit and prospects for Meteosat Second Generation. *Meteorol Appl* 8:23-41
- Nakajima TY, Nakajima T (1995) Wide-area determination of cloud microphysical properties from NOAA AVHRR measurements for FIRE and ASTEX regions. *J Atmos Sci* 52: 4043-4059
- Nauss T (2006) Das Rain Area Delineation Scheme RADS - ein neues Verfahren zur satellitengestützten Erfassung der Niederschlagsfläche über Mitteleuropa. *Marburger Geographische Schriften*, pp 143

- Nauss T, Kokhanovsky AA (2007) Assignment of rainfall confidence values using multispectral satellite data at mid-latitudes: First results. *Adv Geosci* 10:99-102
- Nauss T, Kokhanovsky AA (2006) Discriminating raining from non-raining clouds at mid-latitudes using multispectral satellite data. *Atmos Chem Phys* 6:5031-5036
- Nauss T, Kokhanovsky AA, Nakajima TY, Reudenbach C, Bendix J (2005) The intercomparison of selected cloud retrieval algorithms. *Atmos Res* 78:46-78
- Ou SC, Liou KN, Takano Y, Higgins G, Larsen N, Slonaker R (2002) Cloud Effective Particle Size and Cloud Optical Thickness; Visible/Infrared Imager/Radiometer Suite. Algorithm Theoretical Basis Document
- Ou SC, Liou KN, Gooch WM, Takano Y (1993) Remote Sensing of Cirrus Cloud Parameters using Advanced Very-high-resolution Radiometer 3.7- and 10.9- $\mu\text{m}$  channels. *Appl Optics* 32:2171-2180
- Platnick S, King MD, Ackerman SA, Menzel WP, Baum BA, Riédi JC, Frey RA (2003) The MODIS cloud products: Algorithms and examples from Terra. *IEEE T Geosci Remote* 41:459-473
- Reudenbach C (2003) Konvektive Sommerniederschläge in Mitteleuropa. Eine Kombination aus Satellitenfernerkundung und numerischer Modellierung zur automatischen Erfassung mesoskaliger Niederschlagsfelder. *Bonner Geographische Abhandlungen*, pp 109
- Reudenbach C, Heinemann G, Heuel E, Bendix J, Winiger M (2001) Investigation of summertime convective rainfall in Western Europe based on a synergy of remote sensing data and numerical models. *Meteorol Atmos Phys* 76:23-41
- Rosenfeld D, Gutman G (1994) Retrieving microphysical properties near the tops of potential rain clouds by multispectral analysis of AVHRR data. *Atmos Res* 34:259-283
- Schmetz J, Pili P, Tjemkes S, Just D, Kerkmann J, Rota S, Ratier A (2002) An introduction to Meteosat Second Generation (MSG). *B Am Meteorol Soc* 83:977-992
- Soden BJ, Bretherton FP (1996) Interpretation of TOVS water vapor radiances in terms of layer-average relative humidities: Method and climatology for the upper, middle, and lower troposphere. *J Geophys Res- Atmos* 101:9333-9343
- Stanski HR, Wilson L, Burrows W (1989) Survey of common verification methods in meteorology, World Weather Watch Technical Report No.8. WMO. Geneva. WMO/TD No. 358
- Stone RS, Stephens GL, Platt CMR, Banks S (1990) The Remote Sensing of Thin Cirrus Cloud Using Satellites, Lidar and Radiative Transfer Theory. *J Appl Meteorol* 29: 353-366
- Strabala KI, Ackerman SA, Menzel WP (1994) Cloud Properties Inferred from 8-12- $\mu\text{m}$  Data. *J Appl Meteorol* 33:212-229
- Thies B, Nauss T, Bendix J (2007a) Detection of high rain clouds using water vapour emission - transition from Meteosat First (MVIRI) to Second

- Generation (SEVIRI). Adv Space Res (Submitted)
- Thies B, Nauss T, Bendix J (2007b) Discriminating raining from non-raining cloud areas at mid-latitudes using Meteosat Second Generation SEVIRI night-time data. Meteorol Appl. Accepted for publication.
- Tjemkes SA, van de Berg L, Schmetz J (1997) Warm water vapour pixels over high clouds as observed by Meteosat. Contributions to Atmospheric Physics. 70: 15-21
- Van de Hulst HC (1980) Multiple Light Scattering: Tables, Formulas and Applications. Academic Press. San Diego
- Wu MC (1984) Radiation Properties and Emissivity Parameterization of High Level Thin Clouds. J Clim Appl Meteorol 23:1138-1147
- Turk J, Bauer P (2006) The International Precipitation Working Group and Its Role in the Improvement of Quantitative Precipitation Measurements. B Am Meteorol Soc 87:643-647
- World Weather Research Program/Working Group on Numerical Experimentation Joint Working Group on Verification (WWRP/WGNE): Forecast Verification – Issues, Methods and FAQ, available online at [http://www.bom.gov.au/bmrc/wefor/staff/eee/verif/verif\\_web\\_page.html](http://www.bom.gov.au/bmrc/wefor/staff/eee/verif/verif_web_page.html), 11 May 2007